

# Ultra-short, MeV-scale laser-plasma positron source for positron annihilation lifetime spectroscopy

Thomas L. Audet,<sup>1,\*</sup> Aaron Alejo,<sup>1</sup> Mark Hugh Cunningham,<sup>1</sup> Glenn Ross Frazer,<sup>1</sup> Nasr A. M. Hafz,<sup>2,3,4</sup> Christos Kamperidis,<sup>2</sup> Song Li,<sup>2</sup> Gagik Nersisyan,<sup>1</sup> Daniel Papp,<sup>2</sup> Michael Phipps,<sup>1</sup> Jonathan Richard Warwick,<sup>1</sup> and Gianluca Sarri<sup>1</sup>

<sup>1</sup>*Centre for Plasma Physics, School of Mathematics and Physics, Queen's University Belfast, BT7 1NN, Belfast United Kingdom*

<sup>2</sup>*ELI-ALPS. ELI-HU Non-profit Ltd., H-6728 Szeged, Hungary*

<sup>3</sup>*National Laboratory on High Power Laser and Physics, SIOM, CAS, Shanghai 201800, China*

<sup>4</sup>*Dept. of Plasma and Nuclear Fusion, Nuclear Research Center, Atomic Energy Authority, Abu-Zabal 13759, Egypt*

## Abstract

Sub-micron defects represent a well-known fundamental problem in manufacturing since they significantly affect performance and lifetime of virtually any high-value component. Positron annihilation lifetime spectroscopy is arguably the only established method able to detect defects down to the sub-nanometer scale but, to date, it only works for surface studies, and with limited resolution. Here, we experimentally show that laser-driven positrons, once aptly collimated and energy-selected, can overcome these well-known limitations, by providing ps-scale beams with a kinetic energy tuneable from 500 keV up to 2 MeV and a number of positrons per shot in a 50 keV bandwidth of the order of  $10^3$ . Numerical simulations of the expected performance of a typical mJ-scale kHz laser demonstrate the possibility of generating narrow-band and ultra-short positron beams with a flux exceeding  $10^5$  positrons/s, of interest for fast volumetric scanning of materials at high resolution.

---

\* t.audet@qub.ac.uk

## I. INTRODUCTION

Positron Annihilation Lifetime Spectroscopy (PALS) [1] is arguably one of the most successful techniques for the non-invasive inspection of materials and identification of small-scale defects. PALS presents several unique advantages compared to other inspection techniques: it works virtually with any type of material (crystalline and amorphous, organic and inorganic, biotic and abiotic), it can identify even sub-nanometer defects with concentrations as low as less than a part per million, and it can provide information on the type of defect and its characteristic size. PALS has found applications in testing systems as diverse as turbines, polymers, semiconducting devices, biomimetic systems, zeolites, and solar cells.

Even small-scale defects can have a dramatic effect on the performance and lifetime of high-performance and high-value components, especially when made in, and required to perform under, hostile environments. Heat and pressure treatments, new welding methods, radiation exposure, impact damage, are all examples of scenarios that can leave sub-micron defects in materials during advanced manufacturing or extreme performance use.

In a nutshell, PALS relies on the temporally resolved detection of gamma-rays resulting from the annihilation of positrons as they interact with the material [2]. In a perfect crystal lattice, an implanted positron would rapidly thermalize and subsequently annihilate from a delocalised state. However, a positron is likely to be trapped in the potential induced by a vacancy, such as a missing atomic core [3]. A trapped positron will thus have a more localised state and, therefore, a longer lifetime. The temporal evolution of the gamma-ray emission from the material will thus contain several exponential decays, each with a typical timescale characteristic of the bulk material and of any defects in it. Normally, positron lifetimes in materials are of the order of 200 ps, with longer lifetimes if defects are present (see, for instance, Ref. [2]).

Typical machines designed for PALS routinely operate at a positron energy in the keV range and bunch durations of the order of hundreds of picosecond [4–7]. Despite the high performance of these machines and their wide use for industrial applications and fundamental science, they mainly suffer of two well-known limitations. First, the available positron energy restricts material scanning only to sub-mm depths. Second, the positron bunch duration is relatively long and thus affects the resolution of the technique. For higher resolution, it is preferable to have positron bunch durations that are significantly smaller than the timescales of interest, i.e., at least in the range of a few to tens of ps. In that case, the resolution of the system will be only limited by the detector

response.

These limitations can be overcome if laser-driven positrons are used. Commercially available high power lasers with short pulse durations (fs to ps), can routinely generate high-charge relativistic electron beams of similar duration [8]. The interaction of these electrons with high-Z converter targets can thus produce multi-MeV positron beams with durations in the range of a few to few tens of ps [9–19]. Two main approaches have been identified, based on whether the electrons are generated during direct laser irradiation of the converter target or if they are first generated in a gaseous medium following, for instance, the laser-wakefield acceleration (LWFA) mechanism [8].

Independently of their source, the propagation of high energy electrons through a high Z converter results in the generation of a positron beam. For sufficiently thick converters, two mechanisms are mainly involved: the emission of a high energy photon through bremsstrahlung and the subsequent decay of the photon in electron-positron pairs, with both processes mediated by the nuclear field. Subsequent cascading is also possible, but it is unlikely for sub-radiation length thicknesses [9].

In this article, we show, numerically and experimentally, that positron beams with characteristics appealing to PALS can be produced in a fully-laser driven scenario. First, we experimentally show, using the TARANIS laser hosted by the Centre for Plasma Physics at Queen’s University Belfast [20], that MeV-scale positron beams with a yield of up to  $\sim 7 \times 10^4$  positrons / shot can be obtained. Numerical simulations indicated a positron beam duration at source of the order of a few picoseconds. Implementing a quadrupole doublet system and a dogleg configuration provides sufficient capture and energy-selection of the positron beam so that, at the sample, a positron beam containing a sizeable amount of positrons in a selected energy bandwidth and with a duration of the order of tens of picoseconds can be obtained. Numerical simulations indicate that the same configuration can then be used in conjunction with currently available multi-tens mJ laser systems operating at kHz-scale repetition rates, providing up to  $10^5$  positrons/s in a 50 keV bandwidth, with an energy tuneable from sub-MeV up to a few MeV. Numerical simulations indicate a duration of the beam at the sample plane of the order of 100 ps, thus confirming the feasibility of this system for novel practical applications.

The structure of the article is as follows : Sec. II will describe the main experimental and numerical results concerning positron beam generation and transport using the direct laser-solid interaction scheme. In Sec III we will show numerical results of extending this work to high repetition rate low-energy laser systems. A final discussion of the results presented in this article

and concluding remarks will then be provided in Sec. IV.

## II. POSITRON GENERATION BY DIRECT LASER SOLID IRRADIATION

### A. Experimental setup

The experiments reported in this section were performed using the TARANIS laser facility at the Queen’s University Belfast [20]. A sketch of the experimental setup is shown in Fig. 1.

TARANIS is a chirped pulse amplification (CPA) laser system based on a Ti:Sapphire front-end and a Nd:Glass amplification section. In our experiment, the system delivered laser pulses with an energy of  $E_l = (8.9 \pm 0.5)$  J in a  $\tau_l = (0.8 \pm 0.1)$  ps full width at half maximum (FWHM) pulse duration. The typical intensity contrast of the laser is  $\sim 10^{-7}$  at 1.5 ns before the main pulse. The laser was focused using an F/3 off-axis parabolic mirror (OAP) to a FWHM spot size of  $w_x = (7.6 \pm 0.8)$   $\mu\text{m}$  and  $w_y = (4.9 \pm 0.4)$   $\mu\text{m}$  in the horizontal and vertical directions respectively, leading to a peak intensity on target of  $I_L = (2.5 \pm 0.9) \times 10^{19}$  W/cm<sup>2</sup>. Inset of Fig 1 shows the measured intensity distribution of the laser focal spot in-vacuum. The angle of incidence

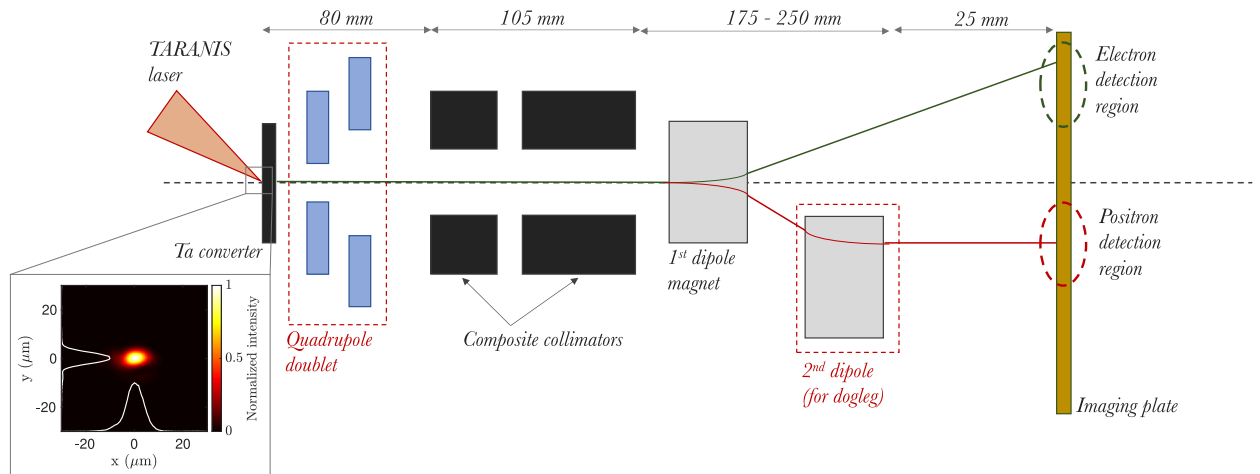


FIG. 1. Sketch of the experimental setup. Three different configurations have been adopted: *full system* (including the quadrupole doublet and the second dipole), *collimation only* (with quadrupole doublet but no second dipole), *generation only* (no quadrupole doublet and no second dipole). Additionally, some shots have been taken with a thin gold target (50  $\mu\text{m}$ ) to measure and characterize the initial electron spectrum starting the positron generation inside the converter.

of the laser beam on the target was  $30^\circ$ .

When focused on a thin target, the pedestal of the laser pulse generates an overdense plasma with a characteristic keV-scale electron temperature. The interaction of the high-intensity peak of the laser with this cold plasma generates a super-thermal population of electrons, with a characteristic temperature of  $T_{hot} \simeq 1$  MeV, which propagates through the target. To experimentally infer the characteristics of this hot electron population, we have performed a series of preliminary shots on thin gold (Au) target with a thickness of  $50\mu\text{m}$ . Fig. 2(a) shows an example of the spectrum of these electrons. The electrons follow a Maxwell-Boltzmann distribution with a temperature of  $k_B T_e \simeq 0.9$  MeV, in agreement with the intensity scalings for the  $\vec{J} \times \vec{B}$  heating mechanism [21]. Here, the total number of detected electrons is  $N_{detected}^{e^-} \simeq 9.5 \times 10^6$ , in a  $6 \times 30$  mrad collection angle. In the full emission cone, the estimated total number of electrons escaping the rear of the Au target is of the order of  $N_{emitted}^{e^-} \simeq 5 \times 10^{10}$ . This electron population will be considered hereafter as a good approximation for the electron population starting the cascade within the thicker converter target. For the rest of the article, we will focus on one specific converter, i.e., a  $l_{Ta} = 2$  mm - thick tantalum foil, corresponding to approximately half of a radiation length.

Different configurations were used after the target, as sketched in Fig. 1. In all the configurations, two collimators were placed on axis, downstream of the target. The collimators are an assembly of plastic, aluminium and lead. The first collimator consists of a  $T_{CH} = 2.25$  mm thick layer of plastic (polyethylene) followed by a  $T_{Al} = 5$  mm thick layer of aluminium (Al), followed by a  $T_{Pb} = 25$  mm thick layer of lead (Pb). The second collimator consists of a  $T_{CH} = 2.25$  mm thick layer of plastic followed by a  $T_{Al} = 5$  mm thick layer of Al, followed by a  $T_{Pb} = 50$  mm thick layer of Pb. Each collimator has a centered circular aperture with a diameter of  $\varnothing_1 = 11$  mm and  $\varnothing_2 = 19$  mm, respectively. In the *generation only* configuration, the collimators are followed by a single dipole magnet with an average field of  $B = 50$  mT and length of 30 mm.

In the *collimation only* configuration, a doublet of quadrupole magnets in the Hallbach configuration (similar to those described in Ref. [22]) was added in between the target and the collimators to increase the collection and collimation of the positrons. Both quadrupoles are 10 mm long and they are separated by 10 mm. Their inner diameters are 44 mm and 88 mm and their magnetic field gradients are 17.8 T/m and 8.95 T/m, respectively.

In the *full system* configuration, a second identical magnetic dipole was added between the first dipole and the detector. This second dipole was placed off-axis, on the positron side to form what is commonly known as a dogleg.

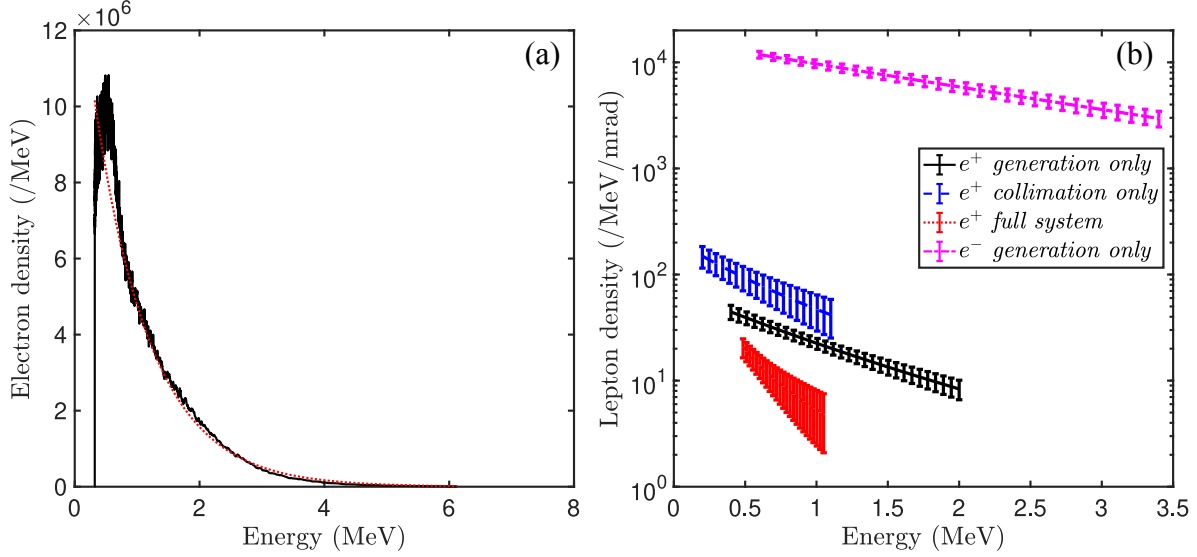


FIG. 2. (a) : Measured electron spectrum (black solid line) and Maxwellian fit (dashed red line) after the interaction of the TARANIS laser (details in the text) with a  $50 \mu\text{m}$  gold target. The collection angle was  $\sim 6$  ( $\sim 30$ ) mrad in the horizontal (vertical) direction, implying a total generated number of electrons of  $\sim 5 \times 10^{10}$ . The Maxwellian fit corresponds to an electron temperature of 0.9 MeV. (b) : Experimental positron spectra obtained using the full system (red dotted line), the quadrupole doublet but no second dipole (blue dashed line), and using no quadrupole and no second dipole (black solid line). The mean electron spectra escaping the solid target in that last configuration is also shown for comparison (dashed dotted magenta line). Error bars are representative of the shot-to-shot standard deviation.

Additional lead shielding (not shown on Fig 1) was used on each side of the collimators to reduce noise at the detector location. In all configurations, electrons, positrons and photons were detected using an imaging plate (IP). The IP used was a BAS-SR2025 (Fuji Film).

## B. Experimental results

During the experiments, several shots in each configuration were taken and the distances between the target, the collimators and the IP were changed. In order to allow for a quantitative comparison between the different configurations, the positron spectra are hereafter normalized by the limiting angle defined by the circular aperture of the collimators in mrad. The angle defined by the diameter of the aperture was varied between 74 and 102 mrad.

Fig. 2(b) shows positron spectra averaged over several shots in the three different configurations, with error bars representative of the shot-to-shot standard deviation; as it can be seen, the positron generation was fairly stable throughout the experiment. To allow for a better comparison, in all cases the averaged spectra are limited to the energy range common to the different realizations. The spectra all exhibit an exponentially decreasing shape and the total number of detected positrons in the different configurations were  $N_{generation}^{e^+} \simeq 3.1 \times 10^3$ ,  $N_{collimation}^{e^+} \simeq 7.2 \times 10^3$  and  $N_{full}^{e^+} \simeq 4.2 \times 10^2$  respectively. Electrons obtained during the same shots as the positrons with no quadrupoles and without the second dipole are also shown as a dashed-dotted magenta line in Fig. 2(b). The electron yield is approximately two orders of magnitude higher than the positron yield in the same configuration.

The performance of the quadrupoles and dogleg is exemplified in Fig. 3(a) as a function of energy, limited to the common energy range; as expected, the addition of the quadrupole doublet leads to an increase of the detected positrons by more than a factor 2. However, the full system, i.e., including the quadrupole doublet and the second dipole to form a dogleg, showed a reduction of the number of positrons detected. The dogleg efficiency varied between 11% and 22%, and it is shown as a function of energy in Fig. 3(b). This relatively low efficiency can be partially explained by the vertical (perpendicular to dispersion plane) limiting angle of the second dipole, which was 5% smaller than the pinholes limiting angle. Another contribution might be the not perfectly dipolar nature of the magnetic field in both of the magnets, as suggested by simulations

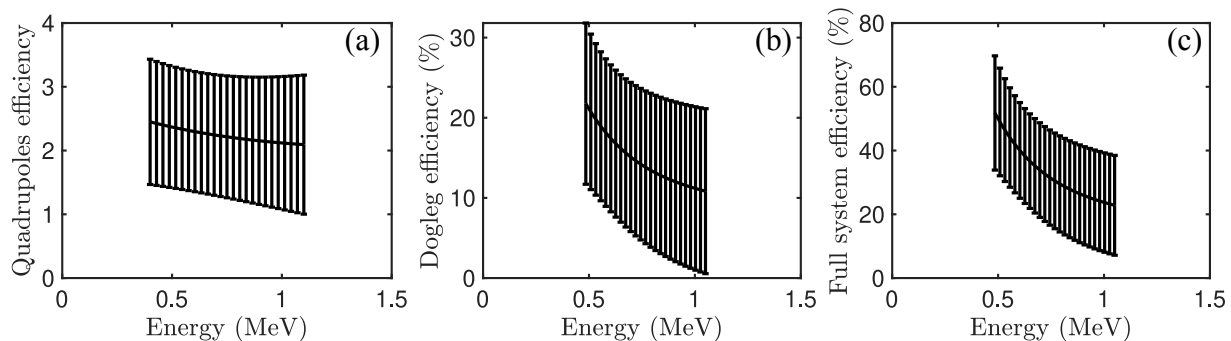


FIG. 3. (a) Ratio between the positron spectrum after collimation (blue dashed line in Fig. 2(b)) and the positron spectrum at source (black solid line in Fig. 2(b)). (b) Ratio between the positron spectrum after the quadrupoles and the dogleg (red dotted line in Fig. 2(b)) and the positron spectrum after the quadrupoles (blue dashed line in Fig. 2(b)). (c) Ratio between the positron spectrum after the quadrupoles and the dogleg (red dotted line in Fig. 2(b)) and the positron spectrum at source (black solid line in Fig. 2(b)).

using ideal dipolar fields (see Sec. II C). Overall, the use of the quadrupoles and dogleg presents a  $\sim 52\%$  to  $\sim 23\%$  capture when comparing the *full system* to the *generation only* configuration as shown in Fig. 3(c).

### C. Numerical Modelling

In order to validate the experimental results discussed in the previous section, numerical modelling of the experiment was performed using the Monte-Carlo code FLUKA [23, 24]. An electron population with a Maxwellian distribution having an electron temperature of 1 MeV was chosen as an input for the simulation (Fig. 4(a)), in agreement with the experimental results using a thin gold (Au) target with a thickness of  $50\mu\text{m}$  (Fig. 2). The simulations were performed with  $2$  to  $4 \times 10^9$  primary electrons and will be scaled up to  $5 \times 10^{10}$  primaries for comparison with experimental results. Due to computational constraints, a pencil-like electron beam with zero temporal duration and a point-like source was assumed.

All previously described configurations were simulated for comparison with the experiment. In all cases, the magnetic dipoles are modelled by an ideal dipolar magnetic field of 50 mT amplitude inside the magnet gap and no magnetic field outside the gap. The quadrupoles are also simulated as ideal quadrupole fields inside the magnets gaps with the gradients corresponding to the experimental values.

Fig. 4(b-d) shows the positron spectra obtained with FLUKA in the three different configurations. In the *generation only* configuration (i.e., no quadrupole doublet and no second dipole), the simulations show the same order of magnitude of positrons as in the experiment (compare Fig. 4(b) and the black solid line in Fig. 2(b)). Similar results are also obtained in the *collimation only* configuration (compare Fig. 4(c) and the blue dashed line in Fig. 2(b)). However, simulation of the full system (red dotted line) shows a higher number of positrons after the dogleg than experimental results. The FLUKA simulations would indicate a dogleg efficiency ranging from 53% at 0.5 MeV to 10% at 1 MeV. This higher efficiency than the experimental values of 11% to 22% (see Sec. II B and Fig. 3(b)) can be partially attributed to idealization of the magnetic fields in FLUKA. Using a custom fortran routine, the particles time of arrival was also scored during these simulations and is displayed in Fig. 5. The blue solid line shows the temporal distribution of the positrons as they exit the target whereas the black dashed line shows their distribution after the dogleg. The positron beam exhibit a  $1/e^2$  time duration of  $\tau_{1/e^2}^{\text{target}} \simeq 5$  ps after the target and  $\tau_{1/e^2}^{\text{dogleg}} \simeq 340$  ps after



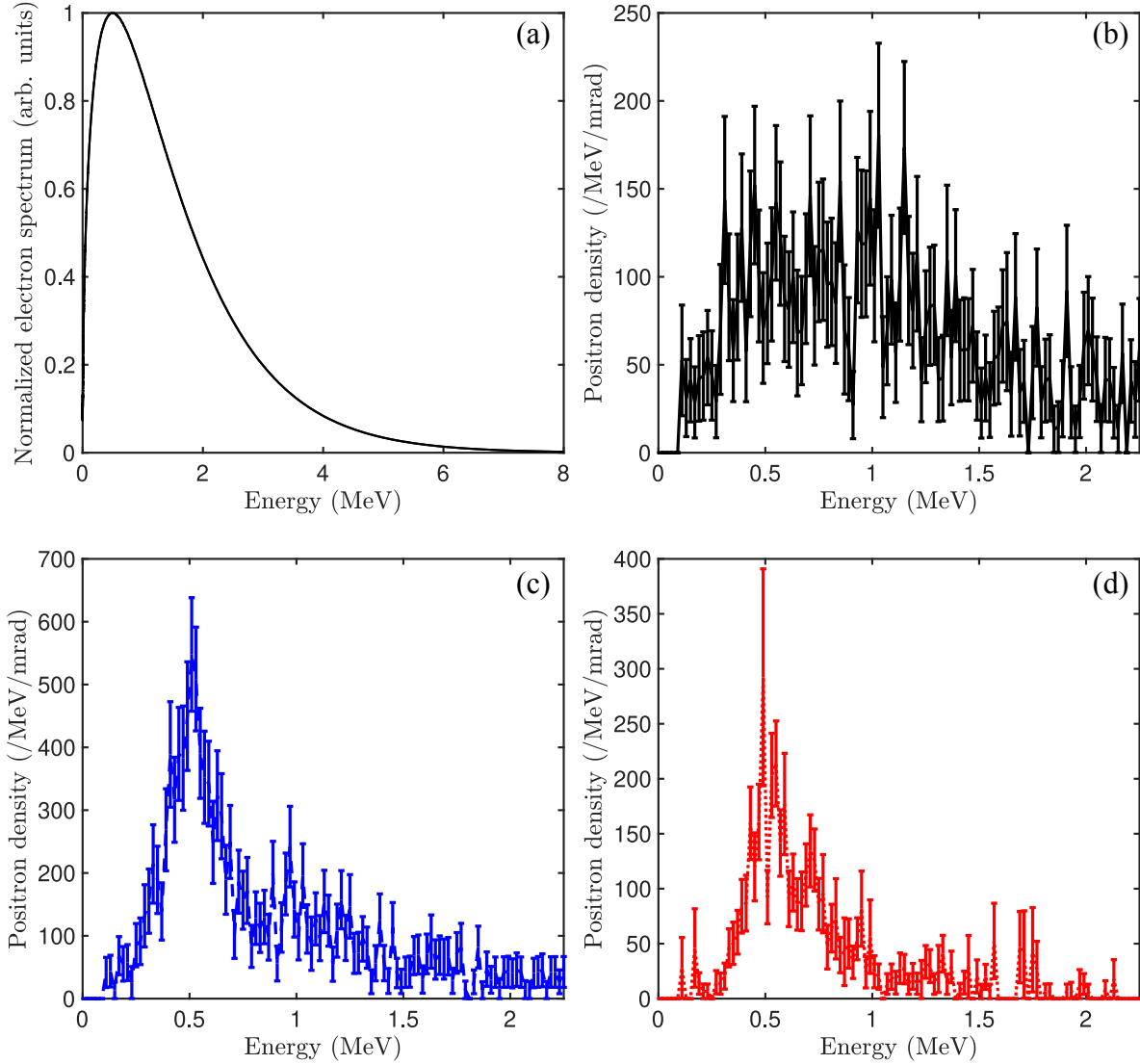


FIG. 4. (a) : Normalized electron energy distribution used as input for FLUKA simulations. (b) : Positron spectra obtained with FLUKA in the *generation only* configuration without quadrupoles or second dipole; (c) in the *collimation only* with quadrupoles but no second dipole and (d) using the full system. (b-d) are using a 2mm thick Ta target.

the dogleg. The broad spectrum of the positrons at source induces different times of flight between the target and the detection plane after the dogleg, as well as different trajectories through the dogleg: these are responsible for the temporal lengthening of the positron beam. It must be noted that these results do not take into account the duration of the primary electron beam at source, which can be estimated as  $\tau_e \simeq 1.2\tau_l \simeq 1$  ps [25] and should be added to the results reported here. The temporal distributions shown in Fig. 5 correspond to the entire positron beam; any energy

selection within the system will result in shorter positron durations at the detector plane. This is because a narrower energy spread would restrict the different paths through the system as well as the temporal spreading due to the different time of flight of positrons with different energies. This will be discussed in more detail in the following section.

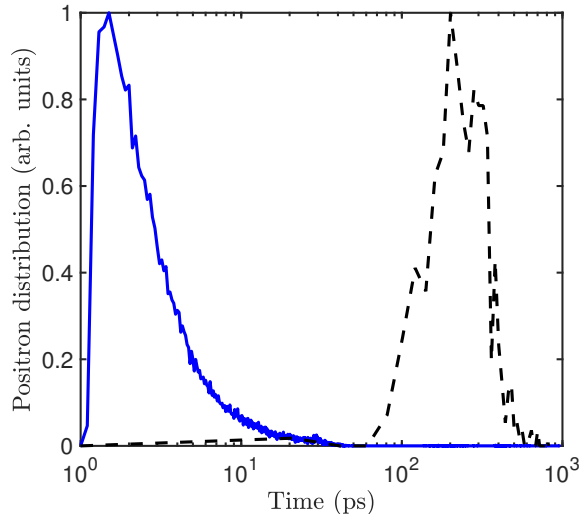


FIG. 5. Positron temporal distributions obtained with FLUKA at the target back surface (blue solid line) and after the dogleg (dashed black line).

### III. EXTENSION TO DIFFERENT LASER SYSTEM : LASER WAKEFIELD ELECTRONS CONVERSION

While the results in Sec. II B & II C demonstrate interesting positron properties, their implementation to practical applications is limited by the typically low repetition rate of Nd:glass high-energy laser systems (approximately a shot every 15 minutes for the TARANIS laser). In the following, these results will be applied to a different approach. This is motivated by the recent availability of TW-scale laser systems with ultra-short (of the order of few fs) pulse duration, and kHz repetition rate. The ultra-short pulse duration of these systems allows them to drive a laser-wakefield accelerator (LWFA) stage able to generate fs electron bunches [8, 26]. As a matter of fact, LWFA electron beams have already been utilized for positron generation experiments [9, 19]. While LWFA electron beams have been limited to electron bunch charges of the order of tens to few hundreds of pC ( $\sim 10^8$  to few  $10^9$  electrons), the increase of repetition rate to the kHz level

and the higher electron energy accessible ( $\gtrsim 1$  MeV), e.g. in [27], will make these upcoming laser systems ideal tools for high flux positron beam generation.

In this section we will use the example of the SYLOS2 laser system which is operational at ELI-ALPS Research Institute in Hungary to study the characteristics of the positron beam such a system could achieve. The SYLOS2 is a 1 kHz-repetition-rate, 4.8 TW optical parametric chirped pulse amplification (OPCPA) laser system that has demonstrated stable long-term operation at 32 mJ output energy and 6.6 fs laser pulse duration at 900 nm central wavelength [28].

### A. Simulations of LWFA electron beam

Numerical simulation of the acceleration was carried out using the EPOCH3D Particle-in-Cell code [29]. The simulation domain was a  $24 \mu\text{m} \times 30 \mu\text{m} \times 30 \mu\text{m}$  moving window with free boundaries, and a mesh resolution on  $50 \text{ nm} \times 200 \text{ nm} \times 200 \text{ nm}$ , with 2 particles per cell. The laser pulse parameters - as expected on-target from the SYLOS2 laser system - were 28 mJ, 7 fs, at 900 nm wavelength, focused to a  $2.2 \mu\text{m}$  FWHM focal spot size for the maximum vacuum intensity of  $3 \times 10^{19} \text{ Wcm}^{-2}$  and  $a_0 = 4.3$ , propagating in the  $x$  direction. The simulated target was pure  $N_2$  gas with a supergaussian profile of order 2.8, with a density "plateau" of  $100 \mu\text{m}$  between 90% density values and  $100 \mu\text{m}$  ramps (between 10% – 90% density values). The laser focused at the start of the plateau (at the first 90% density value). The background electrons from the Nitrogen L-shell were assumed to be pre-ionized, while the two K-shell electrons were non-ionized. Ionization injection was modelled using the EPOCH built-in routines for field, barrier suppression and multiphoton ionization processes. The background electron density of the target was  $6 \times 10^{19} \text{ cm}^{-3}$  corresponding to a plasma wavelength of  $4.3 \mu\text{m}$ .

Fig. 6(a) shows the plasma bubble at the end of the density plateau. At this stage the laser beam is depleted, with  $a_0 \sim 0.2$  for the driving pulse (position shown by white arrow), and the wake is now driven by the first injected electron bunch (orange arrow) due to the very high beam loading. The plasma bubble is significantly elongated, resulting in a  $\sim 10 \mu\text{m}$  long electron bunch length from the continuous injection. Fig. 6(b) shows the longitudinal phase-space of the accelerated electron beam after exiting the plasma ( $180 \mu\text{m}$  after the plateau end). The high-energy (above 18 MeV) tail of the spectrum is entirely from the leading edge of the electron beam. It extends to 60 MeV and has an average energy of 37 MeV and 27 pC of total charge ( $1.7 \times 10^8$  electrons). The low-energy spectrum, with a peak at 3.5 MeV, is from the continuous injection following the

leading bunch, with a total charge of 137 pC ( $8.6 \times 10^8$  electrons). The angular divergence of the electron beam is shown in Fig. 6(d), the low-energy fraction has a FWHM divergence of 115 mrad in the  $y$  (laser polarization) direction and 78 mrad in the  $z$  direction. The high-energy fraction has a smaller divergence, 41 mrad (14 mrad) FWHM in the  $y$  ( $z$ ) direction.

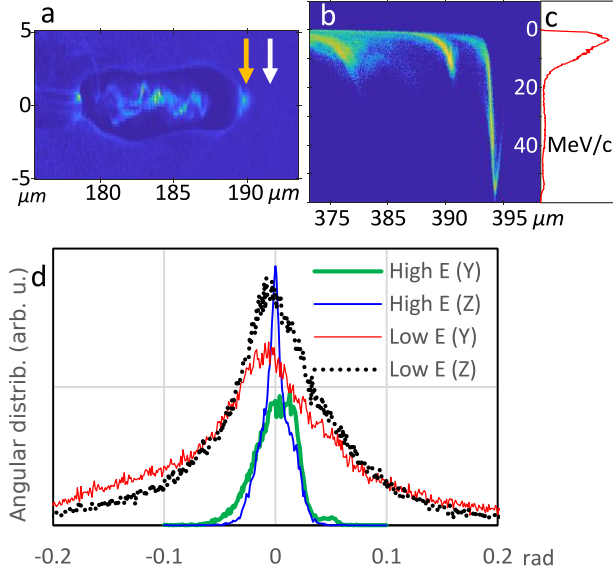


FIG. 6. Plasma density profile snapshot, after transition to beam driven wake, with orange arrow showing the position of the driving electron bunch, and white one showing the position of the laser pulse (a); longitudinal phase-space plot of the injected electrons 90  $\mu\text{m}$  after the plasma (b) and their spectrum (c); and the angular distribution of the high- and low-energy electron population (d) in both transverse directions.

## B. Conversion of LWFA electron beam to positrons

A suitable fitting of the electron spectrum predicted by PIC simulations (see Fig. 7(a)) was used as an input for a FLUKA simulation of the *full system*, i.e., including the 2mm tantalum converter target, the quadrupole magnets, the collimators, and the dogleg. The simulated configuration of the system was identical to the one discussed in Sections II and III, with the only difference that the collection angle was reduced by a factor 2, from 95 mrad to 47.5 mrad.

In order to account for the different divergence angles of the low-energy (below  $\sim 18$  MeV) and high-energy (above  $\sim 18$  MeV) components of the electron spectrum, two different simulations were performed and combined together. The input of the first simulation was an electron beam

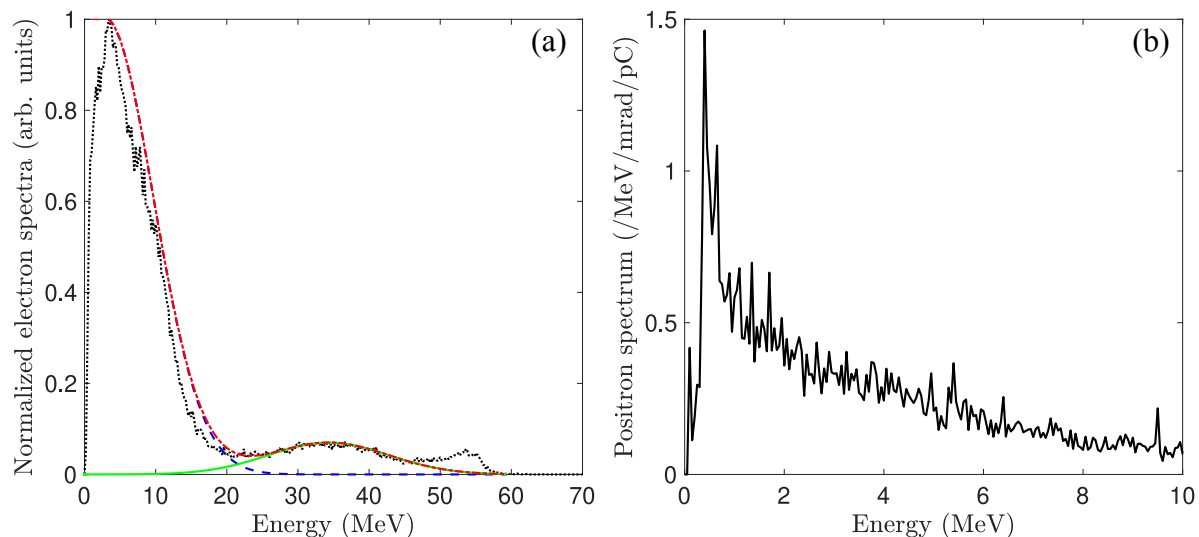


FIG. 7. (a) Normalized electron spectra : expected energy distribution (black dotted line), low energy electron distribution for FLUKA input (blue dashed line), high energy electron distribution for FLUKA input (green solid line), sum of both high and low energy distribution for FLUKA (red dotted dashed line). (b) Positron spectrum after the dogleg, obtained by combination of two FLUKA simulations.

with a low energy distribution exhibiting a gaussian angular distribution with a 100 mrad FWHM width, displayed as a blue dashed line on Fig. 7(a). In a second simulation, the electron beam input, shown on Fig. 7(a) as a solid green line, consisted in a Gaussian energy distribution centered on 35 MeV with a 20 MeV FWHM energy spread and a gaussian divergence of 25 mrad FWHM. Combining and scaling these two simulations resulted in the initial electron distribution shown in Fig. 7(a) as a red dotted dashed line.

The interaction of such an electron beam with a 2mm thick Ta target generated a positron beam which, after collimation and propagation through the magnetic system, resulted in the distribution shown in Fig. 7(b) recorded at the exit of the dogleg. Similarly to what was seen in Sec. II C, the positron distribution after the dogleg is peaked around 500 keV as a consequence of the higher efficiency of the system for this energy.

Fig. 8 shows the temporal distribution of the positron beam after the dogleg for different energy bandwidths. The total positron population has a temporal distribution with a  $1/e^2$  value of  $\sim 230$  ps. As mentioned earlier, restricting the allowed energy bandwidth results in shorter positron beam durations. As an example, allowing only a bandwidth of  $\pm 50$  keV reduces the temporal duration down to a  $1/e^2$  value of  $\sim 90 - 100$  ps (see Fig. 8 and Table I). Even in such a small bandwidth,

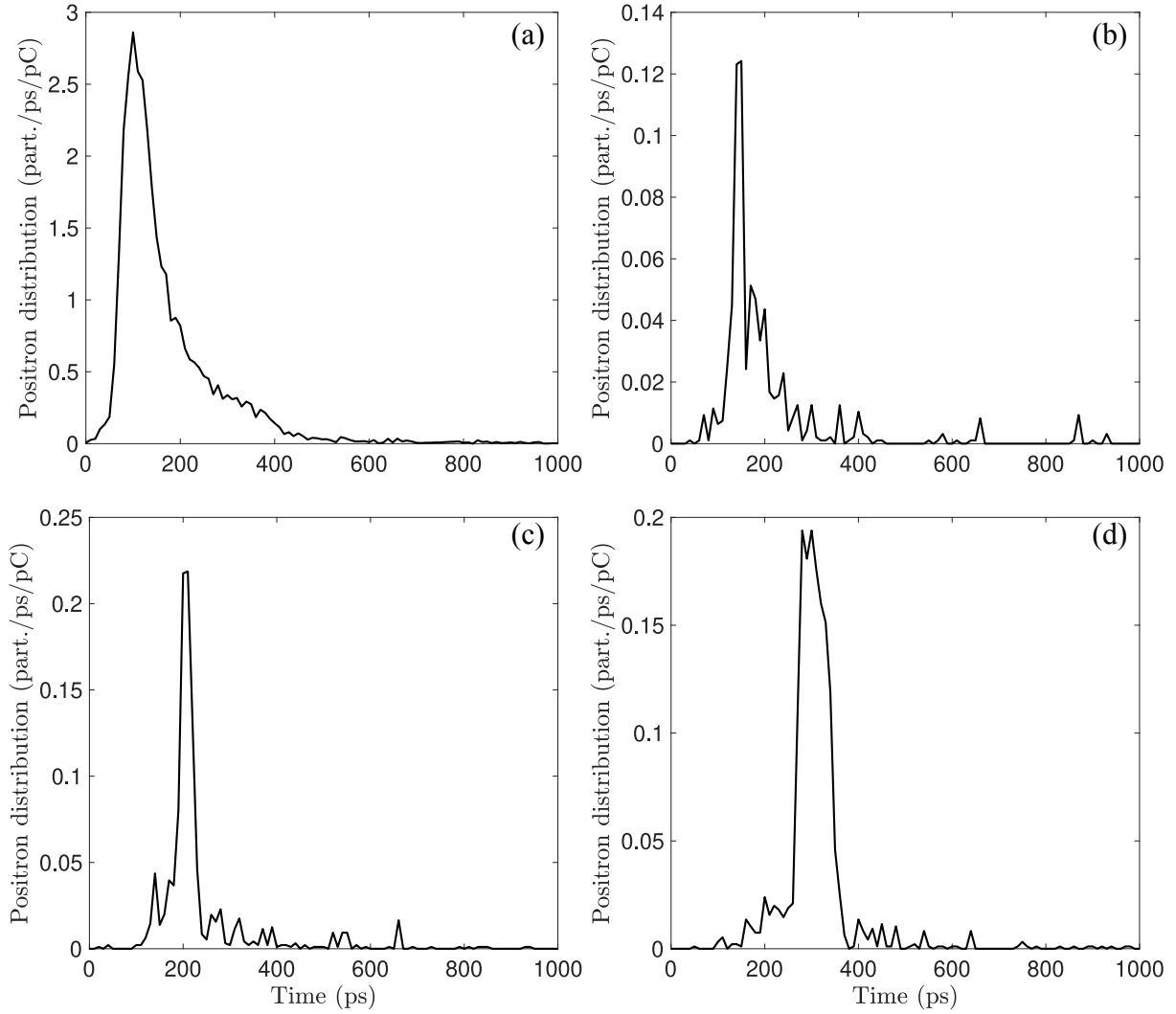


FIG. 8. Temporal distribution of the positrons after the dogleg, for the whole spectrum displayed on 7(a), for positrons with an energy of  $1 \pm 0.05$  MeV (b), for positrons with an energy of  $700 \pm 50$  keV (c), for positrons with an energy of  $500 \pm 50$  keV (d).

the number of positrons escaping the whole system is of the order of 1 – 10 per pC of the primary electron beam per shot. The results, summarised in Table I, would then indicate, for a realistic primary electron beam containing 10 pC of charge, approximately 100 positrons per shot in a 50 keV bandwidth. Operating at 1 kHz repetition rate, this would then translate into more than  $10^5$  positrons per second in a 50 keV bandwidth, well within the requirements for PALS.

Due to the transverse spatial chirp induced by the dogleg on the positron beam, on-shot energy selection can be easily achieved by introducing a moveable slit after the dogleg. This is demonstrated in Fig. 9, which shows the positron energy distribution in different points along the

Energy range	$\tau_{1/e^2}^{dogleg}$ (ps)	$N^{e^+}$			Current ( $e^+/s$ )
		1 pC $e^-$	10 pC $e^-$	150 pC $e^-$	
Whole distribution	230	$\sim 338.4$	$\sim 3384$	$\sim 5.1 \times 10^4$	$\sim 3.4 \times 10^6$
$1 \pm 0.05$ MeV	90	$\sim 7.4$	$\sim 74$	$\sim 1.1 \times 10^3$	$\sim 7.4 \times 10^4$
$700 \pm 50$ keV	100	$\sim 11.0$	$\sim 110$	$\sim 1.7 \times 10^3$	$\sim 1.1 \times 10^5$
$500 \pm 50$ keV	90	$\sim 16.5$	$\sim 165$	$\sim 2.5 \times 10^3$	$\sim 1.5 \times 10^5$

TABLE I. Temporal duration and number of positrons after the dogleg for different energies and different charge of the primary electron beam. The current is given assuming a 10 pC primary electron bunch at a 1 kHz repetition rate.

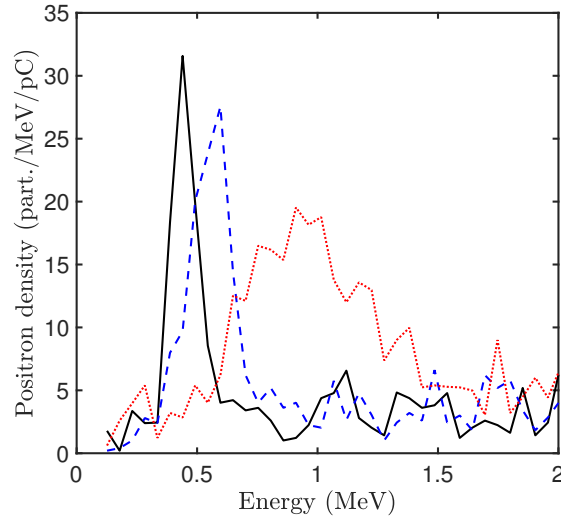


FIG. 9. Example of energy selection after the dogleg. All distributions correspond to a 4.9 mm wide position selection centered on  $\sim 72.0$  mm (black solid line),  $\sim 55.9$  mm (blue dashed line),  $\sim 34.6$  mm (red dotted line) from the main axis.

transverse axis after the dogleg. The position-energy correlation introduced by the dogleg thus allows for energy selection by selecting the position of the slit. In practice, a slit would be placed just after the dogleg to select the required part of the positron spectrum and shield the rest of the beam. In the example shown in Fig. 9, the virtual slit is 4.9 mm wide and select positrons with energies (peak  $\pm$  FWHM) of  $\sim 440 \pm 130$  keV (black solid line),  $\sim 600 \pm 200$  keV (blue dashed line) and  $\sim 910 \pm 630$  keV (red dotted line).

With this setup, the energy selection can be adjusted with the position of the slit and the energy spread can be adjusted with the width of the slit at the expense of the number of positrons reaching the sample. Furthermore, the quadrupoles and dipoles fields could be adjusted to allow a different energy band to go through the dogleg and be selected in the same fashion.

#### IV. DISCUSSION AND CONCLUSIONS

In summary, we report on experimental and numerical studies demonstrating the suitability of laser-driven positron beams as probes for high-resolution and volumetric scanning of materials. Preliminary experiments using the TARANIS laser and a rudimentary beam-line already indicate good efficiency in collection and energy-selection of positrons generated during the interaction of a laser-driven electron beam with a thick tantalum target. Numerically extending these results to the next generation of high repetition rate low-energy laser systems indicates that more than  $10^5$  positrons per second can reach the sample to be probed, with an energy tuneable virtually from zero up to a few MeV, a 50 keV bandwidth, and a duration of the order of 90 - 100 ps. These values are well within the requirements for positron annihilation lifetime spectroscopy studies and provide, for the first time, the possibility of performing volumetric scanning with improved resolution.

It must be noted that the results presented in this paper only used a 2 mm thick Ta target. However, the target thickness can be adjusted with an impact on the positron yield and its duration. For example, preliminary simulations with the same electron input as presented in Fig. 4(a) resulted in a  $\sim 20\%$  increase in the positron yield if a 1 mm thick tantalum converter is used. As a consequence, further optimization of the positron characteristics could be achieved with a scan of the target thickness and a more refined beam-line, which will be the subject of further studies.

#### V. ACKNOWLEDGEMENTS

We acknowledge support from the Engineering and Physical Sciences Research Council (grant numbers: EP/N027175/1, EP/P010059/1, and EP/T021659/1).

Four of the authors (D.P., S.L., C.K., N.A.M.H.) are supported by the European Union through the ELI-ALPS Project under Grant GINOP-2.3.6-15-2015-00001 and in part by Horizon 2020, the EU Framework Programme for Research and Innovation under Grant Agreement No. 654148



and No. 871124 Laserlab-Europe. N. A. M. H. acknowledges the President International Fellowship Initiative (PIFI) of the Chinese Academy of Sciences; the International Partnership Program (181231KYSB20170022) of CAS; the Inter-Governmental Science and Technology Cooperation of MOST.

---

- [1] R. Krause-Rehberg and H. Leipner, *Positron Annihilation in Solids. Defect Studies* (1999).
- [2] D. J. Keeble, S. Wicklein, R. Dittmann, L. Ravelli, R. A. Mackie, and W. Egger, *Physical Review Letters* **105**, 226102 (2010).
- [3] M. J. Puska, C. Corbel, and R. M. Nieminen, *Phys. Rev. B* **41**, 9980 (1990).
- [4] “<https://www.hzdr.de/db/Cms?p0id=35245&pNid=3225>,”.
- [5] “<https://www.hzdr.de/db/Cms?p0id=35320&pNid=3581>,”.
- [6] “<https://www.mlz-garching.de/nepomuc>,”.
- [7] “<https://www.mlz-garching.de/pleps>,”.
- [8] E. Esarey, C. B. Schroeder, and W. P. Leemans, *Rev. Mod. Phys.* **81**, 1229 (2009).
- [9] G. Sarri, W. Schumaker, A. Di Piazza, M. Vargas, B. Dromey, M. E. Dieckmann, V. Chvykov, A. Maksimchuk, V. Yanovsky, Z. H. He, B. X. Hou, J. A. Nees, A. G. R. Thomas, C. H. Keitel, M. Zepf, and K. Krushelnick, *Physical Review Letters* **110**, 255002 (2013).
- [10] G. Sarri, W. Schumaker, A. D. Piazza, K. Poder, J. M. Cole, M. Vargas, D. Doria, S. Kuschel, B. Dromey, G. Grittani, L. Gizzi, M. E. Dieckmann, A. Green, V. Chvykov, A. Maksimchuk, V. Yanovsky, Z. H. He, B. X. Hou, J. A. Nees, S. Kar, Z. Najmudin, A. G. R. Thomas, C. H. Keitel, K. Krushelnick, and M. Zepf, *Plasma Physics and Controlled Fusion* **55**, 124017 (2013).
- [11] G. Sarri, K. Poder, J. M. Cole, W. Schumaker, A. Di Piazza, B. Reville, T. Dzelzainis, D. Doria, L. A. Gizzi, G. Grittani, S. Kar, C. H. Keitel, K. Krushelnick, S. Kuschel, S. P. D. Mangles, Z. Najmudin, N. Shukla, L. O. Silva, D. Symes, A. G. R. Thomas, M. Vargas, J. Vieira, and M. Zepf, *Nature Communications* **6**, 6747 (2015).
- [12] H. Chen, S. C. Wilks, J. D. Bonlie, E. P. Liang, J. Myatt, D. F. Price, D. D. Meyerhofer, and P. Beiersdorfer, *Phys. Rev. Lett.* **102**, 105001 (2009).
- [13] G. Sarri, J. Warwick, W. Schumaker, K. Poder, J. Cole, D. Doria, T. Dzelzainis, K. Krushelnick, S. Kuschel, S. P. D. Mangles, Z. Najmudin, L. Romagnani, G. M. Samarin, D. Symes, A. G. R. Thomas, M. Yeung, and M. Zepf, *Plasma Physics and Controlled Fusion* **59**, 014015 (2016).

- [14] H. Chen, S. C. Wilks, J. D. Bonlie, S. N. Chen, K. V. Cone, L. N. Elberson, G. Gregori, D. D. Meyerhofer, J. Myatt, D. F. Price, M. B. Schneider, R. Shepherd, D. C. Stafford, R. Tommasini, R. Van Maren, and P. Beiersdorfer, *Physics of Plasmas*, **16**, 122702 (2009).
- [15] H. Chen, S. C. Wilks, D. D. Meyerhofer, J. Bonlie, C. D. Chen, S. N. Chen, C. Courtois, L. Elberson, G. Gregori, W. Kruer, O. Landoas, J. Mithen, J. Myatt, C. D. Murphy, P. Nilson, D. Price, M. Schneider, R. Shepherd, C. Stoeckl, M. Tabak, R. Tommasini, and P. Beiersdorfer, *Phys. Rev. Lett.* **105**, 015003 (2010).
- [16] H. Chen, F. Fiuza, A. Link, A. Hazi, M. Hill, D. Hoarty, S. James, S. Kerr, D. D. Meyerhofer, J. Myatt, J. Park, Y. Sentoku, and G. J. Williams, *Phys. Rev. Lett.* **114**, 215001 (2015).
- [17] T. S. Pedersen, J. R. Danielson, C. Hugenschmidt, G. Marx, X. Sarasola, F. Schauer, L. Schweikhard, C. M. Surko, and E. Winkler, *New Journal of Physics* **14**, 035010 (2012).
- [18] E. Liang, T. Clarke, A. Henderson, W. Fu, W. Lo, D. Taylor, P. Chaguine, S. Zhou, Y. Hua, X. Cen, X. Wang, J. Kao, H. Hasson, G. Dyer, K. Serratto, N. Riley, M. Donovan, and T. Ditmire, *Scientific Reports* **5**, 13968 (2015).
- [19] S. Li, G. Li, Q. Ain, M. S. Hur, A. C. Ting, V. V. Kulagin, C. Kamperidis, and N. A. M. Hafz, *Science Advances* **5** (2019), 10.1126/sciadv.aav7940, <https://advances.sciencemag.org/content/5/11/eaav7940.full.pdf>.
- [20] T. Dzelzainis, G. Nersisyan, D. Riley, L. Romagnani, H. Ahmed, A. Bigongiari, M. Borghesi, D. Doria, B. Dromey, M. Makita, S. White, S. Kar, D. Marlow, B. Ramakrishna, G. Sarri, M. Zaka-UI-Islam, M. Zepf, and C. L. S. Lewis, *Laser and Particle Beams*, **28**, 451 (2010).
- [21] W. L. Kruer and K. Estabrook, *The Physics of Fluids*, **28**, 430 (1985).
- [22] T. Eichner, F. Grüner, S. Becker, M. Fuchs, D. Habs, R. Weingartner, U. Schramm, H. Backe, P. Kunz, and W. Lauth, *Phys. Rev. ST Accel. Beams* **10**, 082401 (2007).
- [23] A. Fasso, A. Ferrari, J. Ranft, and P. R. Sala, *FLUKA: a multi-particle transport code*, Tech. Rep. (CERN-2005-10, 2005).
- [24] T. Böhlen, F. Cerutti, M. Chin, A. Fassò, A. Ferrari, P. Ortega, A. Mairani, P. Sala, G. Smirnov, and V. Vlachoudis, *Nuclear Data Sheets* **120**, 211 (2014).
- [25] J. Fuchs, P. Antici, E. d’Humières, E. Lefebvre, M. Borghesi, E. Brambrink, C. A. Cecchetti, M. Kaluza, V. Malka, M. Manclossi, S. Meyroneinc, P. Mora, J. Schreiber, T. Toncian, H. Pépin, and P. Audebert, *Nature Physics* **2**, 48 (2006).
- [26] T. Tajima and J. M. Dawson, *Physical Review Letters* **43**, 267 (1979).

- [27] D. Guénot, D. Gustas, A. Vernier, B. Beaurepaire, F. Böhle, M. Bocoum, M. Lozano, A. Jullien, R. Lopez-Martens, A. Lifschitz, and J. Faure, *Nature Photonics* **11**, 293 (2017).
- [28] S. Toth, T. Stanislauskas, I. Balciunas, R. Budriunas, J. Adamonis, R. Danilevicius, K. Viskontas, D. Lengvinas, G. Veitas, D. Gadonas, A. Varanavičius, J. Csontos, T. Somoskoi, L. Toth, A. Borzsonyi, and K. Osvay, *Journal of Physics: Photonics*, **2**, 045003 (2020).
- [29] T. D. Arber, K. Bennett, C. S. Brady, A. Lawrence-Douglas, M. G. Ramsay, N. J. Sircombe, P. Gillies, R. G. Evans, H. Schmitz, A. R. Bell, and C. P. Ridgers, *Plasma Physics and Controlled Fusion*, **57**, 113001 (2015).